12-16-2016

Ionospheric Signatures of Gravity Waves Produced by the 2004 Sumatra and 2011 Tohoku Tsunamis: A Modeling Study

Michael P. Hickey
Embry-Riddle Aeronautical University, hicke0b5@erau.edu

Yonghui Yu
Nanjing University of Aeronautics and Astronautics, yuyong@nuaa.edu.cn

Wenqing Wang
Nanjing University of Aeronautics and Astronautics

AGU PUBLICATIONS

JGR

Journal of Geophysical Research: Space Physics

RESEARCH ARTICLE
10.1002/2016JA023116

Key Points:
- A 2-D nonlinear time-dependent model displays azimuthally anisotropic gravity waves driven by tsunamis shown in TEC at ionospheric heights
- Incomplete ducting conditions may cast doubt upon a long-range propagating gravity wave afar off the epicenter in the 2004 Sumatra event
- Long-range gravity wave propagation may have been overlooked in the 2011 Tohoku event owning to sparse GPS receivers in the deep Pacific

Correspondence to:
Y. Yu,
yuyong@nuaa.edu.cn

Citation:
Yu, Y., W. Wang, and M. P. Hickey (2017), Ionospheric signatures of gravity waves produced by the 2004 Sumatra and 2011 Tohoku tsunamis: A modeling study, *J. Geophys. Res. Space Physics*, *121*, doi:10.1002/2016JA023116.

Received 28 JUN 2016
Accepted 9 DEC 2016
Accepted article online 16 DEC 2016

Ionospheric signatures of gravity waves produced by the 2004 Sumatra and 2011 Tohoku tsunamis: A modeling study

Yonghui Yu[1], Wenqing Wang[1], and Michael P. Hickey[2]

[1]College of Astronautics, Nanjing University of Aeronautics and Astronautics, Nanjing, China, [2]Department of Physical Sciences and Center for Space and Atmospheric Research, Embry-Riddle Aeronautical University, Daytona Beach, Florida, USA

Abstract Ionospheric fluctuations inferred from observations of total electron content have previously been attributed to tsunamis and have confirmed the strong coupling between Earth's ocean and ionosphere via atmospheric gravity waves (AGWs). To further advance our understanding of this wave coupling process we employ a linear full-wave model and a nonlinear time-dependent model to examine the ionospheric response to the AGW perturbations induced by the 2004 Sumatra and the 2011 Tohoku tsunamis. In the 2004 case, our modeling analyses reveal that one component of the propagating AGWs becomes dynamically unstable in the *E*-region ionosphere at a range exceeding 2000 km in a direction 340° clockwise from north. Another component becomes convectively unstable in the *E*-region ionosphere at a range exceeding 700 km in a direction 250° clockwise from north. In the 2011 case, a significant enhancement in the ionospheric disturbance occurs in a direction northwest from the epicenter about 1 h following the tsunami onset, in general agreement with observations. Our simulations also indicate that the AGW propagating toward the southeast is responsible for a traveling ionospheric disturbance that remains of an observable amplitude for over 4 h during which time it propagates horizontally almost 4000 km.

1. Introduction

Earthquakes often produce fast Rayleigh waves at the Earth's surface, which can in turn produce fast atmospheric acoustic waves that can propagate rapidly to ionospheric heights [e.g., *Liu et al*., 2006, 2011]. Subterranean earthquakes are able to produce tsunamis that in turn can generate obliquely upward propagating atmospheric gravity waves (AGWs), which subsequently disturb the ionosphere thereby creating traveling ionospheric disturbances (TIDs). These can be detected by a variety of techniques, one of which is through the use of the Global Positioning System (GPS) array [e.g., *Rolland et al*., 2010; *Galvan et al*., 2011, 2012; *Occhipinti et al*., 2013; *Crowley et al*., 2016], while others utilize airglow imaging systems [*Makela et al*., 2011; *Smith et al*., 2015].

Lee et al. [2008] postulated that the TID observed over Arecibo on 26 December was a response to the AGW induced by the 2004 Sumatra tsunami. Shown in their Figure 7, *Lee et al*. [2008] proposed two different possible scenarios. In the first scenario, tsunami-induced AGWs propagate between Sumatra (3.316°N, 95.854°E) and Puerto Rico (18.5°N, 66°W) along a great circle path of about 18,000 km; the AGWs are imperfectly ducted for a long distance, and wave energy ultimately leaks into the ionosphere over Arecibo. In the second scenario, the AGWs over Arecibo are generated locally by nearby tsunami waves (the latter having traveled from the epicenter along a large U-turn path first across the Indian Ocean, then into the Atlantic Ocean), and propagate in the northwest direction over Arecibo.

The 2011 Tohoku tsunami occurred in an area densely distributed with a GPS array, providing an excellent opportunity to study the ionospheric response to a tsunami by monitoring the total electron content (TEC) [e.g., *Komjathy et al*., 2012; *Galvan et al*., 2012]. Previous tsunami-ionosphere studies have shown that the ionospheric response broadly depends on the latitude where the tsunami occurred and the direction of wave travel [e.g., *Artru et al*., 2005a, 2005b; *Occhipinti et al*., 2006, 2008]. *Hickey et al*. [2009] found that the ionospheric response to the 2004 Sumatra tsunami would be most favorable for tsunami propagation in the meridional direction. This dependence is due to a significant coupling between neutrals and ions that maximizes along the geomagnetic field direction near the equator [*Occhipinti et al*., 2008].

Previous GPS observations in regions close to the epicenter have revealed that the TEC fluctuations associated with the 2011 Tohoku tsunami were largest for waves propagating toward the northwest of the

epicenter [*Galvan et al*., 2012]. It has been suggested that this remarkably different ionospheric response for different wave propagation directions is due to the different ocean depths associated with the two different directions of wave travel: slower (horizontal phase speed c) gravity waves are generated for propagation toward shallow coastal waters and faster (c) gravity waves are generated for propagation toward the deep ocean [*Yu et al*., 2015]. Horizontal mean winds indeed play a vital role in the upward propagation of gravity waves. The zonal wind can significantly impact the ability of zonally propagating waves to reach higher altitudes [*Yu et al*., 2015], while the typically weaker meridional wind has less effect on meridionally propagating waves, although it can impact the efficiency of the coupling between the gravity wave and the plasma [*Occhipinti et al*., 2008; *Hickey et al*., 2009].

Recently, *Vadas et al*. [2015] modeled the excitation of AGWs by the localized vertical body force of an ocean surface wave packet . They derived linear solutions in an isothermal, windless, and nondissipative atmosphere. One of their significant findings is that some of the excited AGWs may have greater phase speeds than that of the ocean surface wave. This finding was used to explain observations of *Makela et al*. [2011], in which some "early" AGW signatures were observed in the airglow layer an hour before the Tohoku tsunami reached Hawaii.

The purpose of this paper is to further quantitatively evaluate the dependence of the ionospheric response near the earthquake epicenters to propagation directions for the 2004 Sumatra and 2011 Tohoku tsunami events. In so doing, we will improve our understanding with regard to the evolution of tsunami-generated gravity waves and subsequent TEC variations over time and space. There is a solid evidence for tsunamigenic gravity waves propagating in the ionosphere [e.g., *Lee et al*., 2008; *Galvan et al*., 2012; *Crowley et al*., 2016], but their dissipation and contribution to the turbulence at ionospheric altitudes are still largely unknown. In this paper we determine whether the tsunamigenic gravity waves eventually break into turbulence and, if so in what form (dynamical or convective) that instability would take. In so doing, we are able to adequately distinguish the range of area that the waves affect in the ionosphere and retrospectively link the simulations to the observations by *Lee et al*. [2008] and *Galvan et al*. [2012]. We prospect the simulated ionospheric response to be a plausible bound to such tsunamigenic gravity waves (medium-scale, horizontal wavelength λ_h ~hundreds of kilometer) [*Occhipinti et al*., 2008; *Hickey et al*., 2009]. Although rarely seen elsewhere in TEC observations, small-scale AGWs (λ_h ~ tens of kilometer) are sometimes observed to break down in airglow images [e.g., *Yamada et al*., 2001].

Analyses of the height dependence of wave amplitudes are first performed by using a full-wave model [*Hickey et al*., 2009] for a nonisothermal atmosphere with the inclusion of viscosity and mean winds. Second, the neutral-ion coupling is studied in detail by using a 2-D time-dependent nonlinear model [*Yu and Hickey*, 2007a; *Yu et al*., 2009] that has been modified to include ion chemistry and dynamics. The simulated ionospheric response associated with each of the two tsunami events is presented in terms of the vertical TEC (V-TEC) and/or the electron number density, and we will investigate how these relate to previous observations.

The paper is arranged as follows. The numerical models, one of which includes ion chemistry and dynamics, are described in section 2. The ambient mean atmosphere near the two earthquake epicenters is described in section 3. The wave parameters and the model forcing are described in section 4. The results of the wave simulation are provided in section 5 and are followed by a discussion and conclusions in sections 6 and 7, respectively.

2. Numerical Models

2.1. Full-Wave Model

The first model is a high-resolution 1-D, linear, steady state full-wave model [*Hickey et al*., 1997]. Note that a spectral version of the full-wave model (not used here) has been previously used by *Hickey et al*. [2009] to study tsunami-driven gravity wave packet propagation in the atmosphere associated with the 2004 Sumatra tsunami. The effects of these waves on the ionosphere were also modeled [*Hickey et al*., 2009]. In follow-up studies, the effects of these waves on mesospheric and thermospheric airglow emissions were studied [*Hickey et al*., 2010a], and the nonlinear interaction of these waves with the mean state was also examined [*Hickey et al*., 2010b]. In the present study we do not use this version of the full-wave

model, but instead rely on the nonlinear 2-D model (section 2.2) to describe the upward propagation of AGW packets.

The full-wave model solves the complete linearized equations of continuity, momentum, and energy for a compressible, viscous, and thermally conducting atmosphere with the effects of ion drag and Coriolis force, and with realistic altitude variations of the basic temperature and wind structure. At the upper boundary a radiation condition is imposed using the dispersion equation of *Hickey and Cole* [1987].

2.2. 2-D Model

The second model is a 2-D, nonlinear, time-dependent gravity wave model that incorporates ion chemistry and dynamics. The model has been previously used to study gravity wave propagation in the atmosphere [*Yu and Hickey*, 2007a, 2007b, 2007c; *Yu et al*., 2009, 2015]. The model solves the Navier-Stokes equations with an explicit Lax-Wendroff scheme and an implicit Newton-Raphson scheme for wave propagation in a nonisothermal, viscous atmosphere in the presence of background winds. Rayleigh friction and Newtonian cooling are imposed as a sponge layer near the upper boundary of the model [*Walterscheid and Schubert*, 1990], while lateral boundaries are periodic over a horizontal wavelength to simulate a horizontally infinite domain.

Coded in the 2-D model, the hydromagnetic momentum equation (1) is solved for the ions O^+, N_2^+, O_2^+, and NO^+, which are influenced by collisional coupling with neutral perturbations produced by tsunami-induced AGWs. This equation, with the ion continuity equation (2) and the equation (3) for charge neutrality, governs the ion dynamics [*Kelley*, 1989]. Note that a similar approach to include ion dynamics has been applied by *Occhipinti et al*. [2008] to study the ionospheric response to tsunami-induced AGWs.

$$\rho_j \frac{d\vec{v_j}}{dt} = -\underline{\nabla} p_j + \rho_j \vec{g} + n_j q_j \left(\vec{E} + \vec{v_j} \times \vec{B}\right) - \rho_j \upsilon_{jn} \left(\vec{v_j} - \vec{v_n}\right) \tag{1}$$

$$\frac{\partial n_j}{\partial t} + \underline{\nabla} \cdot \left(n_j \vec{v_j}\right) = P_j - n_j L_j \tag{2}$$

$$n_e = \sum_{j=1}^{4} n_j \tag{3}$$

Here ρ_j, p_j, n_j, q_j, and $\vec{v_j}$ are the jth ion density, pressure, number density, charge, and velocity, respectively; $\vec{v_n}$ is the neutral velocity; $\upsilon_{jn} = 2.6 \times 10^{-15}(n_n + n_j)A^{-1/2}$ [*Kelley*, 1989] is the collision frequency between an ion and neutrals; n_n is the neutral number density; A is the mean neutral molecular mass. The $\vec{g}$, $\vec{E}$, and $\vec{B}$ are the gravity, the electric and magnetic fields, respectively. P_j and L_j are the chemical production and loss rates for the jth ion, respectively; n_e is the electron number density.

The magnetic field vector $\vec{B}$ is related to the magnetic dip angle I [*Hickey et al*., 2009]:

$$\vec{B}/B = \vec{i}\cos I + \vec{k}\sin I. \tag{4}$$

The dipole angle I is related to latitude θ with a simple dipole field assumption.

$$\sin I = -2\sin\theta/\sqrt{1 + 3\sin^2\theta}, \tag{5}$$

$$\cos I = -\cos\theta/\sqrt{1 + 3\sin^2\theta} \tag{6}$$

where $\vec{i}$ and $\vec{k}$ are positive due southward and upward, respectively. We prescribe the electric field $\vec{E}$ in equation (7) so that the forcing term $\vec{K}$ becomes independent of $\vec{B}$ for gravity wave propagation [*Occhipinti et al*., 2008].

$$\vec{K} = -\underline{\nabla} p_j + \rho_j \vec{g} + n_j q_j \vec{E} = -\rho_j \upsilon_{jn} \vec{v_n} \tag{7}$$

The numerical method to solve the ion densities is straightforward. Following the neutral dynamics solution for each time step, we first solve the ion equation (1) to calculate the ion velocity $\vec{v_j}$, and then apply the second order explicit Lax-Wendroff scheme in the ion continuity equation (2), which is rewritten as a partial differential equation in a flux-preserved form. All ion number densities n_j (O^+, N_2^+, O_2^+, and NO^+) are individually solved with respect to time. Finally, we use the ion equation (3) to obtain the electron number density (n_e) and calculate the time-resolved V-TEC by integrating n_e over altitude.

Table 1. Chemical Reactions for Ions (k_j, the Chemical Reaction Rate, $m^3\ s^{-1}$; T, Temperature, K)

Chemical Reaction	Reaction Rate
$O^+ + N_2 \rightarrow NO^+ + N$	$k_1 = 5\times10^{-19}$
$O^+ + O_2 \rightarrow O_2^+ + O$	$k_2 = 2\times10^{-17}(300/T)^{0.4}$
$O^+ + N_2 \rightarrow N_2^+ + O$	$k_{2a} = 2\times10^{-17}(300/T)^{0.4}$
$O^+ + NO \rightarrow NO^+ + O$	$k_3 = 8\times10^{-19}$
$O^+ + e \rightarrow O(^5P) + h\nu_{1356}$	$k_4 = 7.3\times10^{-19}$
$O_2^+ + N_2 \rightarrow NO^+ + NO$	$k_5 = 5\times10^{-22}$
$O_2^+ + N \rightarrow NO^+ + O$	$k_{5a} = 1.2\times10^{-16}$
$O_2^+ + NO \rightarrow NO^+ + O_2$	$k_6 = 4.4\times10^{-16}$
$O_2^+ + e \rightarrow O + O$	$k_7 = 1.6\times10^{-13}(300/T)^{0.55}$
$N_2^+ + O \rightarrow NO^+ + N$	$k_8 = 1.4\times10^{-16}(300/T)^{0.44}$
$N_2^+ + O \rightarrow O^+ + N_2$	$k_9 = 1\times10^{-17}(300/T)^{0.23}$
$N_2^+ + O_2 \rightarrow O_2^+ + N_2$	$k_{10} = 5\times10^{-17}(300/T)$
$N_2^+ + NO \rightarrow NO^+ + N_2$	$k_{11} = 3.3\times10^{-16}$
$N_2^+ + e \rightarrow N + N$	$k_{12} = 1.8\times10^{-13}(300/T)^{0.39}$
$NO^+ + e \rightarrow N + O$	$k_{13} = 4.2\times10^{-13}(300/T)^{0.85}$

The ion chemistry is applied from *Schunk and Sojka* [1996] with some reaction rates acquired from *Rees* [1989]. The atomic and molecular ions O^+, N_2^+, O_2^+, and NO^+ are produced by charge exchange processes and lost by emission and dissociative recombination processes (Table 1). Their chemical production and loss rates (P_j and L_j, respectively) are presented in Table 2. Note that similar ion chemistry has been applied by *Hickey et al*. [2009] to study the ionospheric response to the 2004 Sumatra tsunami.

3. Ambient Mean Atmosphere

The ambient neutral atmosphere is described by the Mass Spectrometer and Incoherent Scatter-90 (MSIS-90) model [*Hedin*, 1991] for the mean conditions prevailing at the epicenter location of the 11 March 2011 Tohoku tsunami, for a latitude and longitude of 38.322°N and 142.369°E, respectively, and for a universal time of 05 h 46 m. This model is also used to define the mean conditions prevailing at the epicenter for the 26 December 2004 Sumatra tsunami, for a latitude and longitude of 3.316°N and 95.854°E, respectively, and for a universal time of 0 h 58 m. The solar and geomagnetic activities appropriate to the time of the 2004 event are moderately active ($A_p = 12$; $F_{10.7} = 88.7$ and its 81 day mean is 102.8) [*Hickey et al*., 2009]. We are aware that there was an enhanced geomagnetic activity during the time of the 2011 event [*Komjathy et al*., 2012], and so we apply slightly higher solar and geomagnetic conditions for it ($A_p = 48$; $F_{10.7} = 121.5$ and its 81 day mean is 104.4) (ftp://ftp.ngdc.noaa.gov/STP/GEOMAGNETIC_DATA/INDICES/KP_AP/). To facilitate a consistency (or perhaps a comparison) with previous studies [*Hickey et al*., 2009; *Yu et al*., 2015], the horizontal mean winds are incorporated by using the Horizontal Wind Model-93 [*Hedin et al*., 1996] using the same input parameters as provided above.

Horizontal mean winds can profoundly influence upward wave propagation, leading to anisotropic wave propagation and thereby leading to characteristics (such as intrinsic wave period and vertical wavelength) that depend on propagation direction in the thermosphere. Figure 1a shows the mean wind profiles related to the 2004 Sumatra tsunami. The meridional wind is small below 100 km altitude and approaches 30 m/s northward by 500 km altitude. The zonal wind is about 20 m/s westward near the stratopause (45 km). At higher altitudes it increases, reaching a local maximum of about 50 m/s eastward near 110 km altitude, and then about 54 m/s westward near 132 km altitude. At greater heights it reaches about 75 m/s eastward by 500 km altitude.

We also plot the mean winds projected in the N250°E and N340°E directions (Figure 1a), each defined by a rotation of 250° and 340° clockwise from the north, respectively. These two directions are inferred from the directions of two major ocean surface wave propagations associated with the tsunami event [*Abe*, 2006]. It can be seen that over most altitudes the N250°E wind is significantly larger than the N340°E wind.

Table 2. Chemical Production (P_j, $m^{-3}\ s^{-1}$) and Loss Rates (L_j, s^{-1})

	Loss rate	Production rate
O^+	$(k_1 + k_{2a})N_2 + k_2O_2 + k_3NO + k_4e$	$k_9ON_2^+$
N_2^+	$(k_8 + k_9)O + k_{10}O_2 + k_{11}NO + k_{12}e$	$k_{2a}N_2O^+$
O_2^+	$k_5N_2 + k_{5a}N + k_6NO + k_7e$	$k_2O_2O^+ + k_{10}O_2N_2^+$
NO^+	$k_{13}e$	$k_1N_2O^+ + k_3NOO^+ + k_5N_2O_2^+ + k_{5a}NO_2^+ + k_6NOO_2^+ + k_8ON_2^+ + k_{11}NON_2^+$

Altitude profiles of the sound speed, mean temperature, and Brunt-Väisälä period (τ_B) near the 2004 Sumatra epicenter are shown in Figure 1b. The temperature reaches an exospheric temperature of about 750 K at high altitudes. Above about 120 km altitude τ_B increases with

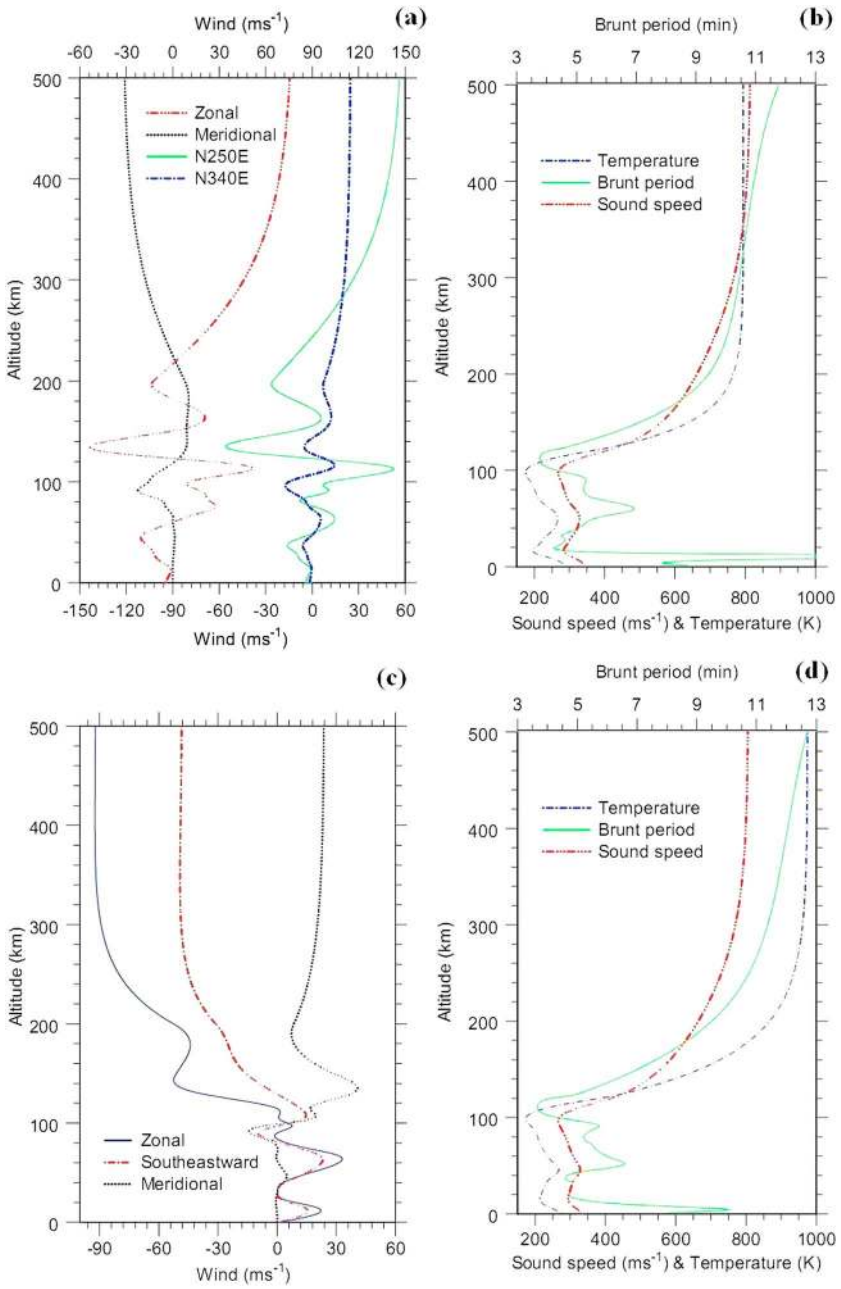

Figure 1. Horizontal mean winds positive toward the east (zonal), south (meridional), and southeast (upper *x* axis) and negative in the N250°E and N340°E directions (lower *x* axis) ((a) Sumatra and (c) Tohoku). Brunt-Väisälä period (upper *x* axis), sound speed and mean temperature (lower *x* axis) ((b) Sumatra and (d) Tohoku).

height, leading to a filtering of the shortest-period waves. τ_B is about 10.5 min near the *F*-region peak (300 km) [*Hickey et al*., 2009; *Galvan et al*., 2012], so that waves having periods longer than this are expected to dominate. The sound speed has two local minima near 20 and 100 km altitude with values of about 280 m/s.

The horizontal mean winds, mean temperature, sound speed, and Brunt-Väisälä period near the 2011 Tohoku epicenter are shown in Figures 1c and 1d for reference. A detailed description of the atmospheric variables plotted in Figures 1c and 1d is not presented here, but they have been described before by *Yu et al*. [2015].

The mean profile of the electron number density ($n_e(z)$) is modeled as a Chapman layer with the F_2 peak (300 km) [*Hickey et al*., 2009; *Galvan et al*., 2012] and an *E*-layer peak (105 km) with a respective maximum

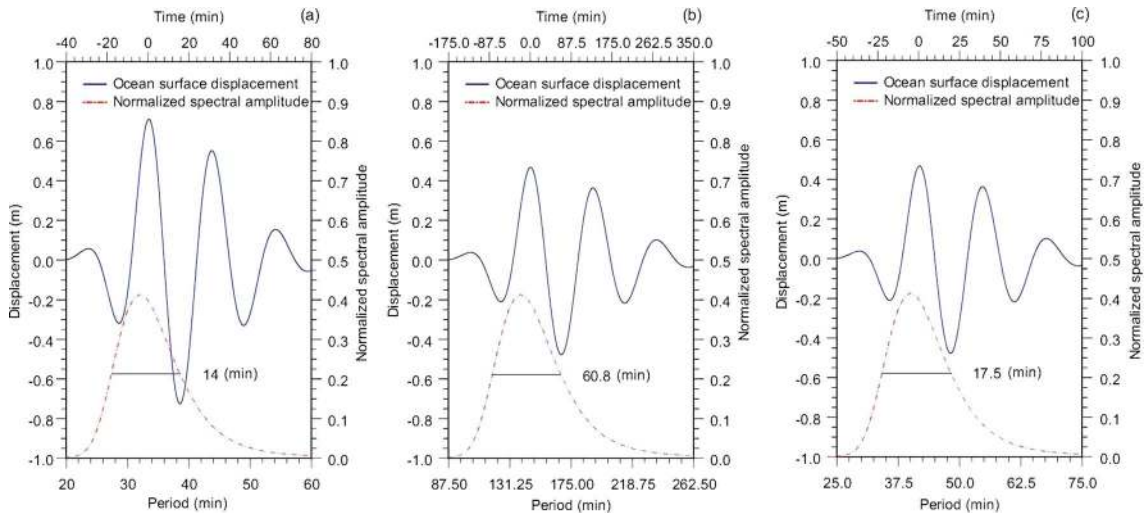

Figure 2. Ocean surface displacement ξ (equation (10), $x = 0$) (solid line, upper x axis, left y axis) and normalized spectral amplitude (dashed dotted line, lower x axis, right y axis) at the 2011 Tohoku epicenter [*Yu et al.*, 2015] ((a) $\tau_c = 0$ min, $\tau_d = 32$ min, FWHM = 14 min, $\tau = 20$–60 min, $\chi = 120$ min) and at the 2004 Sumatra epicenter ((b) N340°E, $\tau_c = 0$ min, $\tau_d = 139$ min, FWHM = 60.8 min, $\tau = 87$–262 min, $\chi = 525$ min; (c) N250°E, $\tau_c = 0$ min, $\tau_d = 40$ min, FWHM = 17.5 min, $\tau = 25$–75 min, $\chi = 150$ min).

number density of 1.17×10^{12} m^{-3} and 1.47×10^{7} m^{-3} for the tsunami events. This assumption implies a condition of moderate solar activity. The Chapman layer is defined by

$$n_e(z) = N_{\max} \exp\left\{0.5\left[1 - \frac{(z - z_{\max})}{H} - \exp\left(-\frac{(z - z_{\max})}{H}\right)\right]\right\} \tag{8}$$

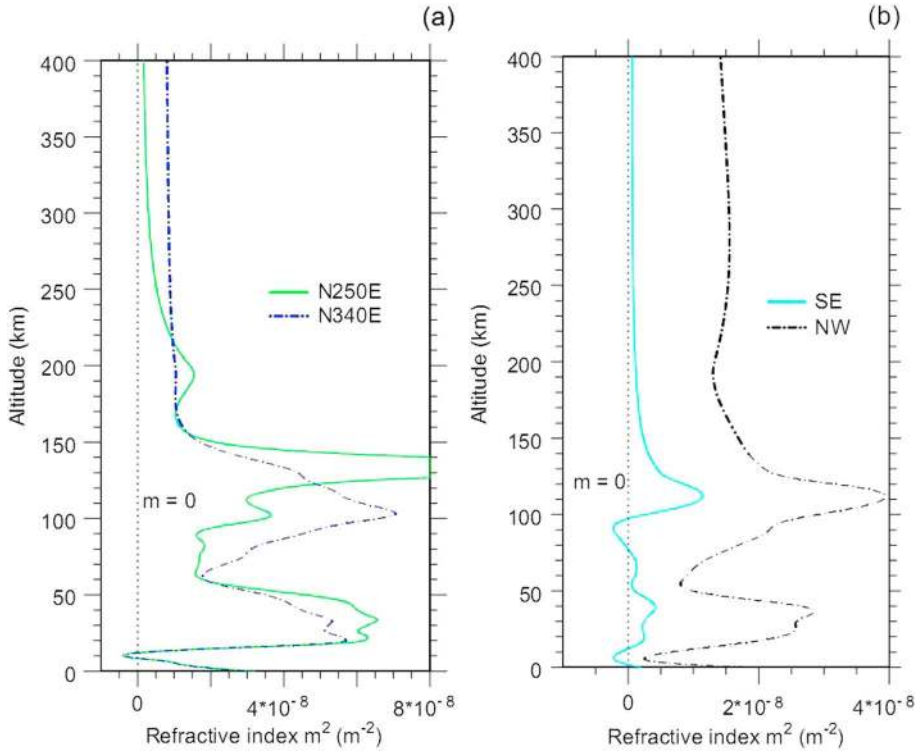

Figure 3. Refractive indexes (a) for the 40 and 139 min (τ_d) waves, respectively, propagating toward the N250°E and N340°E directions ($\lambda_h = 238$ and 826 km) driven by the 2004 Sumatra tsunami and (b) for the 32 min (τ_d) waves, respectively, propagating toward the southeast and northwest ($\lambda_h = 466.56$ and 232.32 km) driven by the 2011 Tohoku tsunami.

where z_{max} and N_{max} are the height and value of the maximum number density, respectively, and H is the atmospheric scale height at the E-region or F-region peak. The TEC mean value was calculated by integrating $n_e(z)$ (8) over altitude. It was about 21 and 17 total electron content unit (TECU) at the Tohoku and Sumatra epicenters, respectively, where 1 TECU = 10^{16} el m^{-2}.

We solve for the mean number densities of O^+, $N_2{}^+$, and $O_2{}^+$ by neutralizing charge to eliminate NO^+, and then following *Hickey et al*. [2009] solve the matrix equation below with chemical rate coefficients supported by *Schunk and Sojka* [1996] (Tables 1 and 2).

$$\begin{bmatrix} L(O^+) & -k_9O & 0 \\ k_1N_2 + k_3NO + k_{13}n_e & k_8O + k_{11}NO + k_{13}n_e & k_5N_2 + k_{5a}N \\ & & +k_6NO + k_{13}n_e \\ -k_2O_2 & -k_{10}O_2 & L(O_2{}^+) \end{bmatrix} \begin{bmatrix} O^+ \\ N_2{}^+ \\ O_2{}^+ \end{bmatrix} = \begin{bmatrix} 0 \\ k_{13}n_e{}^2 \\ 0 \end{bmatrix} \quad (9)$$

The mean number density profiles of the neutral species were acquired from the MSIS-90 model [*Hedin*, 1991] except for NO, which was modeled as a Gaussian profile with a maximum number density of 10^{14} m^{-3} at 115 km altitude and with a full width at half maximum (FWHM) of about 42 km [*Hickey et al*., 2009]. This is a good representative profile based on the empirical model of *Marsh et al*. [2004].

4. Wave Parameters and Forcing

Tsunami travels at the shallow-water wave speed ($\sqrt{gh}$) that depends on the gravity (g) and the ocean depth (h) [*Holton*, 2012]. For wave propagation toward the northwest of the Tohoku epicenter (shallow coastal waters, average depth about 1.5 km), the shallow-water wave speed was about 121 m/s. Deep-ocean Assessment and Reporting of Tsunamis (DART) allows measurement of the average speed of a tsunami between the epicenter and the ocean buoys. DART buoy no. 21419 measured an average wave speed of about 243 m/s southeastward [*Galvan et al*., 2012]. The wave amplitude of the sea surface height was about 0.76 m (A_m), and the dominant wave period was about 32 min (τ_d) [*Galvan et al*., 2012]. The horizontal wavelength λ_h (and associated phase speed c) was about 232.32 km (121 m/s) for the northwestward propagating wave and about 466.56 km (243 m/s) for the southeastward propagating wave.

Abe [2006] discussed the tide gauge records associated with the 2004 Sumatra tsunami and found that the N340°E direction was associated with the direction of fault strike, for which the dominant wave period (τ_d) was about 139 min and the horizontal wavelength (λ_h) was about 826 km. The N250°E direction was associated with the normal fault, for which τ_d was about 40 min and λ_h was about 238 km. These periods were derived from tide gauge measurements, while the horizontal wavelengths λ_h were derived from a horizontal phase speed equal to the local shallow-water wave speed (99 m/s) for an average sea depth of about 1 km [*Abe*, 2006].

4.1. Full-Wave Model Forcing

In the steady state full-wave model the wave of 32 min period (τ_d) for the 2011 Tohoku tsunami is forced at sea level with vertical velocity amplitude of about 2.49×10^{-3} m/s (= ωA_m, where ω is the extrinsic wave frequency and A_m is the maximum surface displacement of 0.76 m) [*Galvan et al*., 2012].

For the 2004 Sumatra tsunami, the wave of 139 min period (τ_d, λ_h = 826 km, c = 99 m/s) propagating toward the fault strike (N340°E) and the wave of 40 min period (τ_d, λ_h = 238 km, c = 99 m/s) propagating toward the normal fault (N250°E) are forced with vertical velocity amplitudes of about 3.77×10^{-4} and 1.31×10^{-3} m/s, respectively (A_m = 0.5 m) [*Hickey et al*., 2009].

4.2. 2-D Model Forcing

Forcing in the 2-D model is implemented by prescribing a time-dependent vertical displacement ξ at the lower boundary (sea level), which is applied to the right-hand side of the vertical momentum equation (Appendix A of *Yu et al*. [2015]). Following *Yu et al*. [2015], it is described analytically as a traveling sinusoidal wave modulated by a Gaussian envelop over time,

$$\xi(x, 0, t) = A_m \exp\left(-(t - \tau_c)^2 / 2\Delta t^2\right) \sin(k_0 x - \omega_0 t). \quad (10)$$

Here x is the horizontal position and t is the time. The remaining parameters are the maximum ocean surface displacement (A_m, Tohoku: 0.76 m, Sumatra: 0.5 m), the center time (τ_c, Tohoku: 05 h 46 m UT, Sumatra: 0 h 58 m UT), the Gaussian depth of time ($\Delta t = \tau_d/2$ before τ_c, $\Delta t = \tau_d$ after τ_c), a horizontal wave number ($k_0 = 2\pi/\lambda_h$), and an extrinsic frequency ($\omega_0 = 2\pi/\tau_d$), respectively, for the 2004 and 2011 cases.

The spectral amplitude for each wave period is normalized by partitioning a fraction of the total power amplitude. For the 2011 case, the wave source is derived with a maximum normalized spectral amplitude of about 0.42 at 32 min (τ_d) and with a FWHM of about 14 min (Figure 2a) [*Yu et al*., 2015]. This ocean surface wave packet composes a continuum spectrum of periods (τ) ranging from 20 to 60 min and a duration (χ) of 120 min (Figure 2a). This is a good representative wave configuration based on the DART measurements [*Galvan et al*., 2012] and previous simulations [*Yu et al*., 2015].

For the 2004 case, we similarly derive the wave source with a maximum normalized spectral amplitude of about 0.42 at 139 min (τ_d) and with a FWHM of about 60.8 min for the N340°E wave (Figure 2b). The ocean surface wave packet in this direction composes a continuum spectrum of periods (τ) ranging from 87 to 262 min and a duration (χ) of 525 min. For the N250°E direction, we also derive the wave source with a maximum normalized spectral amplitude of about 0.42 at 40 min (τ_d) and with a FWHM of about 17.5 min (Figure 2c). The ocean surface wave packet in the direction composes a continuum spectrum of periods (τ) ranging from 25 to 75 min and a duration (χ) of 150 min. Each wave packet propagates horizontally with one monochromatic wavelength (λ_h) [*Yu et al*., 2015; *Vadas et al*., 2015]; most gravity wave components of the spectrum lie within a range of $\pm 21\%$ centered about the dominant wave period (τ_d) (Figure 2).

Vadas et al. [2015] found largest momentum flux for the fundamental excited gravity waves, and only those consistent with the sole λ_h of an ocean surface wave packet are significant and nonnegligible. Here we approximate the horizontal group velocity of the gravity wave packet with the horizontal dominant phase speed (c) [*Salmon*, 2014, p. 27]. We configure those ocean surface wave packets close to the epicenters according to exact measures by *Abe* [2006] and *Galvan et al*. [2012] and sound modeling by *Yu et al*. [2015] unless otherwise noted.

5. Results of Wave Simulation

In this section we present from the full-wave model the altitude variations of the refractive index, and the amplitudes of the temperature and velocity perturbations, for the dominant (monochromatic) wave in the source spectrum. From the 2-D model, we present the V-TEC time variations of the ionospheric response, resulting from an entire source spectrum as discussed before, and the atmospheric stability.

5.1. Full-Wave Model Results

The square of the vertical wave number m^2, the so-called refractive index, determines the wave propagation. It obeys the dispersion equation [*Gossard and Hooke*, 1975]

$$m^2 = \frac{\left(N^2 - \Omega^2\right)\left(k^2\right)}{\left(\Omega^2 - f^2\right)} + \frac{\Omega^2}{{C_s}^2} - \frac{1}{4H^2}. \tag{11}$$

Here N is the nonisothermal Brunt-Väisälä frequency, Ω is the wave intrinsic frequency ($\Omega = \omega - k\bar{U}$), k is the horizontal wave number, $\bar{U}$ is the horizontal mean wind in the direction of wave propagation, f is the inertial frequency, C_s is the sound speed, and others are as defined previously.

Figure 3 shows the refractive indexes for the gravity waves driven by the 2004 Sumatra and 2011 Tohoku tsunamis. The waves propagating toward the N250°E and N340°E directions (Sumatra tsunami, $c = 99$ m/s; Figure 3a) remain internal ($m^2 > 0$) in most regions except for a narrow region of evanescence ($m^2 < 0$) in the upper troposphere. These waves become evanescent due to the thermal structure of this region (large atmospheric lapse rate, see Figure 1b). The wave propagating toward the southeast (Tohoku tsunami, $c = 243$ m/s; Figure 3b) exhibits regions of evanescence ($m^2 < 0$) in the lower and middle troposphere and also in the upper mesosphere. The wave propagating toward the northwest (Tohoku tsunami, $c = 121$ m/s; Figure 3b) remains internal ($m^2 > 0$) everywhere. The Tohoku waves have been previously discussed by *Yu et al*. [2015].

These results indicate that the upward propagation should be partially impeded for the southeastward propagating wave in the lower and middle troposphere, mainly due to the fact that its intrinsic phase speed

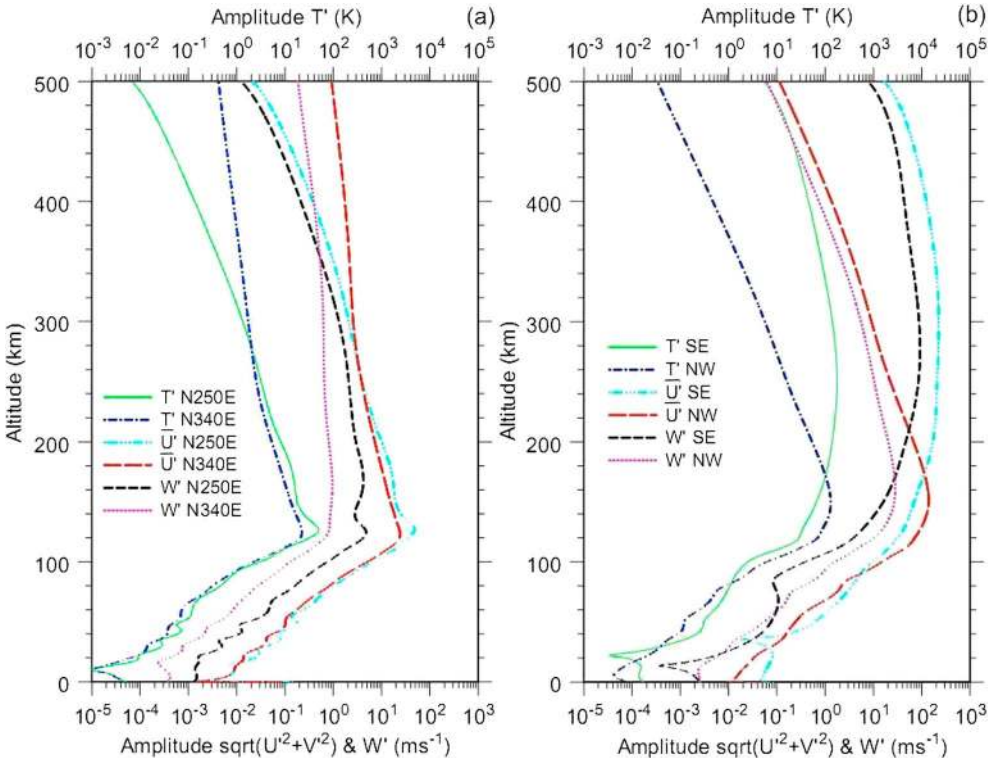

Figure 4. Amplitudes of the temperature (upper *x* axis), horizontal and vertical velocity perturbations (lower *x* axis) for the waves (a) propagating toward the N250°E and N340°E directions driven by the 2004 Sumatra tsunami and (b) propagating toward the southeast and northwest driven by the 2011 Tohoku tsunami.

($c - \bar{U} = 243 - 16 = \sim 227$ m/s, c is the extrinsic phase speed, $\bar{U}$ is the southeastward mean wind, see Figure 1c) exceeds about 0.8 of the local sound speed (about 280 m/s, see Figure 1d). An evaluation of the limited wave intrinsic phase speed compared to the local sound speed for internal gravity waves can be found in the works of *Walterscheid and Hickey* [2011] and *Yu et al.* [2015]. The northwestward wave does not experience evanescence and its propagation to the ionosphere occurs freely.

Figure 4a shows perturbation amplitudes for the temperature T', the horizontal velocity U' and the vertical velocity W', and for wave propagation toward the N250°E and N340°E directions near the 2004 Sumatra epicenter. For both waves, the T' amplitude grows with height up to about 120 km altitude. Undulations in the amplitude below this height are mainly associated with weak reflections from the base of the thermosphere. The two waves have an identical extrinsic phase speed ($\overrightarrow{V_e} = \omega/k$) (about 99 m/s), but different intrinsic phase speeds ($\overrightarrow{V_i} = \Omega/k$) due to the mean wind ($\overrightarrow{V_i} = \overrightarrow{V_e} - \overrightarrow{U}$). In the region directly below about 120 km altitude, the refractive index for the N340°E wave is larger than that for the N250°E wave (see Figure 3a). The larger refractive index equates to smaller vertical wavelength (λ_z) which in turn results in greater viscous dissipation. This explains the slightly smaller amplitude of the wave propagating in the N340°E direction at altitudes directly above this region (at altitudes of 120 to 130 km shown in Figure 4a).

In the 120 to 220 km altitude range, the N250°E wave, which is slower and therefore has a smaller value of λ_z (and a larger refractive index, see Figure 3a), experiences a larger viscous dissipation rate than does the N340°E wave (see Figure 4a). Consequently, by about 280 km altitude the temperature amplitudes of the two waves become equal. Above 280 km altitude the N340°E wave has a larger temperature amplitude than does the N250°E wave because the refractive index for the N250°E wave asymptotes to $m = 0$, and it becomes marginally evanescent (see Figure 3a) so that its upward propagation is partially impeded. Consequently, by 500 km altitude the N340°E wave achieves a temperature perturbation amplitude of about 0.4 K, while the N250°E wave only achieves a temperature perturbation amplitude of about 0.007 K (see Figure 4a).

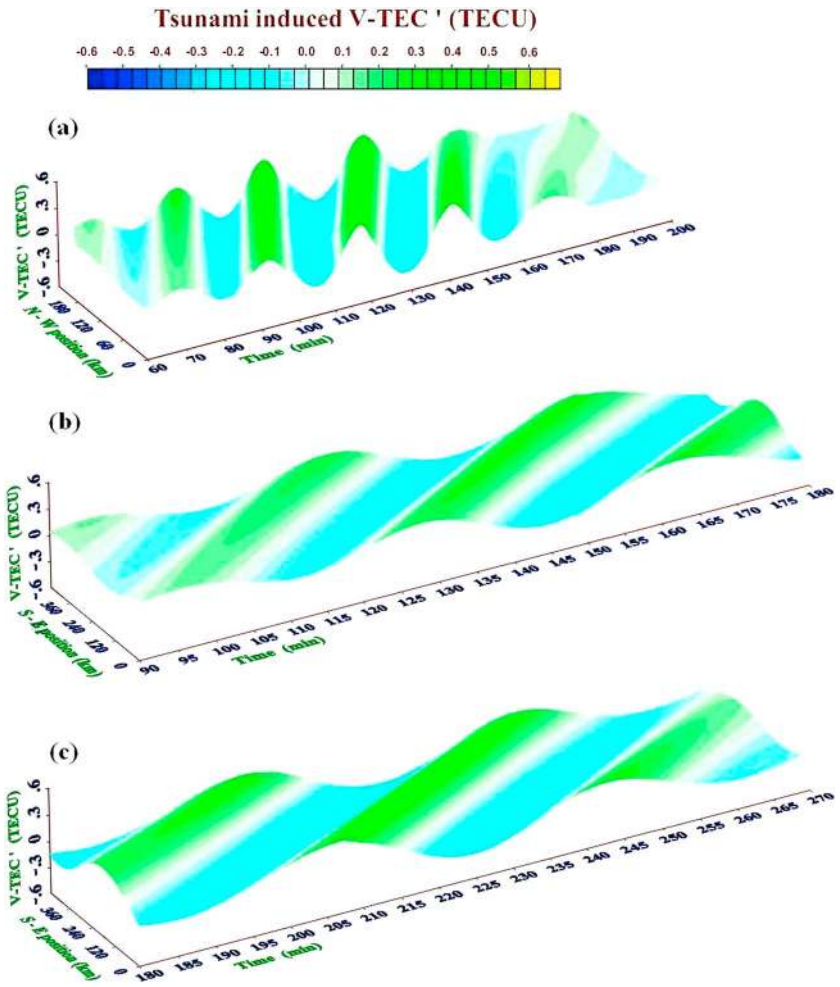

Figure 5. V-TEC perturbations (mean: 21.3 TECU) due to AGWs propagating toward the (a) northwest ($\lambda_h = 232.32$ km, $\tau_d = 32$ min, $c = 121$ m/s) and (b and c) southeast ($\lambda_h = 466.56$ km, $\tau_d = 32$ min, $c = 243$ m/s) driven by the 2011 Tohoku tsunami.

Amplitudes of the horizontal velocity perturbations U' for the waves propagating in the N250°E and N340°E directions are also shown in Figure 4a. U' for the N250°E wave has a maximum value of about 50 m/s at about 120 km altitude, larger than U' (about 20 m/s) for the N340°E wave in this region. For the reasons discussed previously, U' for the N250°E wave decreases more rapidly with height in the thermosphere, achieving about 0.02 m/s by 500 km altitude. For the N340°E wave the decrease of U' is more modest, and this wave achieves an amplitude of about 1 m/s by 500 km altitude.

Amplitudes of the vertical velocity perturbation W' for the two waves are also shown in Figure 4a. Their variations with altitude tend to follow the corresponding altitude variations of their U' values, but W' is smaller than the corresponding U' by a factor of approximately $k/m \approx \tau_B/T_i$, where $\tau_B = 2\pi/N$ is the Brunt-Väisälä period, $T_i = 2\pi/\Omega$ is the intrinsic wave period, and others are as defined previously. This factor is typically about 0.1, as can be seen in Figure 4a. Note that while the amplitudes of U' are similar for the two waves, the values of W' are not. This is explained as follows. The forcing of the waves in W' provides a displacement $\zeta = W'/i\omega = 0.5$ m [*Hickey et al*., 2009] and so because the two waves have different frequencies their vertical velocities are different. However, for low-frequency gravity waves $W' \approx -\omega U'/N$ [*Hickey and Cole*, 1987], which leads immediately to the result that $|\zeta| \approx |U'|/N$. Hence, U' is approximately the same for the two waves.

Altitude variations of the amplitudes of T', U', and W' for the southeastward and northwestward waves associated with the Tohoku event are shown here in Figure 4b for reference. A detailed analysis of their propagation properties has been described before and can be found in *Yu et al*. [2015].

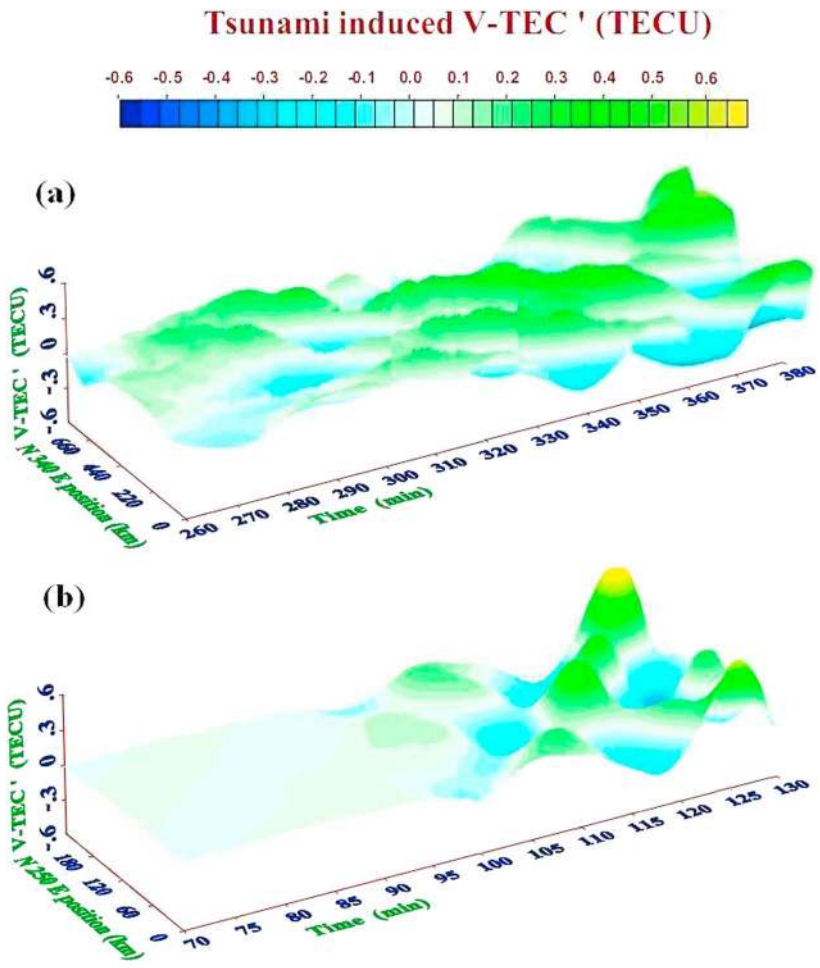

Figure 6. V-TEC perturbations (mean: 17.2 TECU) due to AGWs propagating toward the (a) N340°E ($\lambda_h = 826$ km, $\tau_d = 139$ min, $c = 99$ m/s) and (b) N250°E directions ($\lambda_h = 238$ km, $\tau_d = 40$ min, $c = 99$ m/s) driven by the 2004 Sumatra tsunami.

Note that for the wave propagating in the N250°E direction driven by the 2004 Sumatra tsunami, the maximum temperature amplitude is about 50 K near 125 km altitude (see Figure 4a), approximately 12.5% of the mean (400 K, see Figure 1b). The corresponding amplitude of the horizontal velocity fluctuation is about 50 m/s near 125 km altitude (see Figure 4a). The *Orlanski and Bryan* [1969] criterion for the onset of convective instability is that $U' > c'$ where U' is the horizontal wind perturbation and c' is the intrinsic horizontal phase speed. For this wave the intrinsic phase speed is equal to the extrinsic phase speed minus the horizontal wind speed ($c - \underline{V} = 99 - 54 = \sim 45$ m/s near 125 km altitude; Figure 1a), which is less than the maximum value of U' (~50 m/s) near 125 km altitude. Because $U' > c'$, this wave amplitude exceeds the threshold amplitude required for the onset of convective instability. Therefore, we expect that the wave propagating in the N250°E direction associated with the 2004 Sumatra tsunami would achieve convective instability while propagating upward through the 125 km altitude region.

5.2. 2-D Model Results

The V-TEC is calculated at each horizontal position and at each time of the 2-D model by integrating n_e over altitude. In Figures 5 and 6, we show these V-TEC fluctuations as a function of time and horizontal position across the grid. The horizontal positions vary from zero to one complete horizontal wavelength, and the times shown are with respect to the times of the tsunami onset (Tohoku: 05 h 46 m UT; Sumatra: 0 h 58 m UT).

5.2.1. 2011 Tohoku

The results presented in Figure 5 are for the 2011 Tohoku tsunami and for the 32 min wave packets propagating toward the northwest ($\lambda_h = 232.32$ km; Figure 5a) and southeast ($\lambda_h = 466.56$ km;

Figures 5b and 5c). The TEC mean value for this case is about 21.3 TECU. In Figure 5a we see a wavy packet propagating toward the northwest, with a local maximum of about 0.45 TECU (~2 % of the mean) occurring at about 125 min after the tsunami onset. Apparently, four or five cycles of significant V-TEC fluctuations occur at times between about 60 and 200 min after the tsunami onset, spanning a horizontal extent between about 436 and 1452 km ($\approx \lambda_h * t/\tau_d$) from the epicenter.

Figures 5b and 5c show another wave packet propagating toward the southeast. The V-TEC fluctuations exhibit a local maximum of about 0.35 TECU (~1.6 % of the mean) occurring at a time of about 230 min. Four or five cycles of significant V-TEC fluctuations appear at times between about 90 and 270 min after the tsunami onset and span a horizontal extent between about 1312 and 3937 km ($\approx \lambda_h * t/\tau_d$) from the epicenter. The V-TEC amplitudes gradually increase with increasing time up to about 230 min, after which they decrease.

A comparison of the results for the two waves shown in these figures demonstrates that the V-TEC fluctuations for the 2011 Tohoku tsunami are stronger and occur earlier for the wave propagating toward the northwest than for the wave propagating toward the southeast. In the former case the V-TEC fluctuations reach a value of about 0.45 TECU about 2 h following the tsunami onset, whereas in the latter case the V-TEC fluctuations reach a value of about 0.35 TECU about 4 h following the tsunami onset. Analyses of these V-TEC fluctuations for the 2011 Tohoku tsunami show that after 1 h following the tsunami onset, the TID activity northwest of the epicenter is stronger (northwest: 0.06 TECU, southeast: 0.02 TECU). This result agrees with the observations of *Galvan et al*. [2012] and with the previous simulations of *Yu et al*. [2015] that focused on the gravity waves themselves. According to the simulations of *Yu et al*. [2015], the northwest wave significantly perturbs the *E*-region ionosphere sooner (after 1 h following the tsunami onset) than does the southeast wave, causing the TEC fluctuations to occur earlier (see Figure 5a). The northwest wave also significantly disturbs the *F*-region ionosphere sooner (after about 2 h) than does the southeast wave (after about 4 h) (electron number density fluctuations, not shown). Although the southeast wave has an observable V-TEC fluctuation of about 0.2 TECU at near 120 min (see Figure 5b), this occurrence has not been confirmed by observations, such as those of *Galvan et al*. [2012], most probably because of the sparsely populated GPS receiver network toward the southeast of the epicenter.

5.2.2. 2004 Sumatra

The V-TEC fluctuations associated with the 2004 Sumatra tsunami are presented in Figure 6. The results for the 139 min wave packet propagating in the N340°E direction ($\lambda_h = 826$ km) are shown in Figure 6a, and those for the 40 min wave packet propagating in the N250°E direction ($\lambda_h = 238$ km) are shown in Figure 6b. The TEC mean value for this case is about 17.2 TECU. We observe that in Figure 6a the 139 min wave packet propagating in the N340°E direction leads to instability and breaks into turbulence at about 378 min (a horizontal distance of about $\lambda_h * t/\tau_d \approx$ 2246 km in the far field). A local maximum of about 0.5 TECU (~3 % of the mean) occurs at about 372 min. Figure 6b shows that the 40 min wave packet propagating in the N250°E direction leads to instability and breaks into turbulence at about 130 min (a horizontal distance of about $\lambda_h * t/\tau_d \approx$ 773 km in the far field). A local maximum of about 0.67 TECU (~4 % of the mean) occurs at about 126 min.

We present three pairs of comparison between the N340°E and N250°E waves in Figure 7 to show wave breakdown characteristics. Wave breakdown can be partially supported by an altitude-time contour plot of the relative fluctuations of electron number density ($(n_e - \overline{n_e})/\overline{n_e}$) (so-called factor change in Figure 7). For the N340°E wave at position 544 km, Figure 7a shows that two local maxima and one local minimum of about 1, 0.7, and −0.7 occur at approximate 338, 358, and 378 min, respectively, and at near 170 km altitude. Figure 7b indicates for the N250°E wave at position 224 km that two local maxima of about 8 and 24 occur at about 120 and 130 min, and at altitudes close to 170 and 180 km, respectively.

Additionally, a time series of the V-TEC perturbations is presented for AGWs propagating toward the N340°E direction at position 544 km (Figure 7c) and toward the N250°E direction at position 224 km (Figure 7d). After initial sinusoidal oscillations, at later times (N340°E: about 360 min, N250°E: about 125 min) their amplitudes increase significantly and become more turbulent.

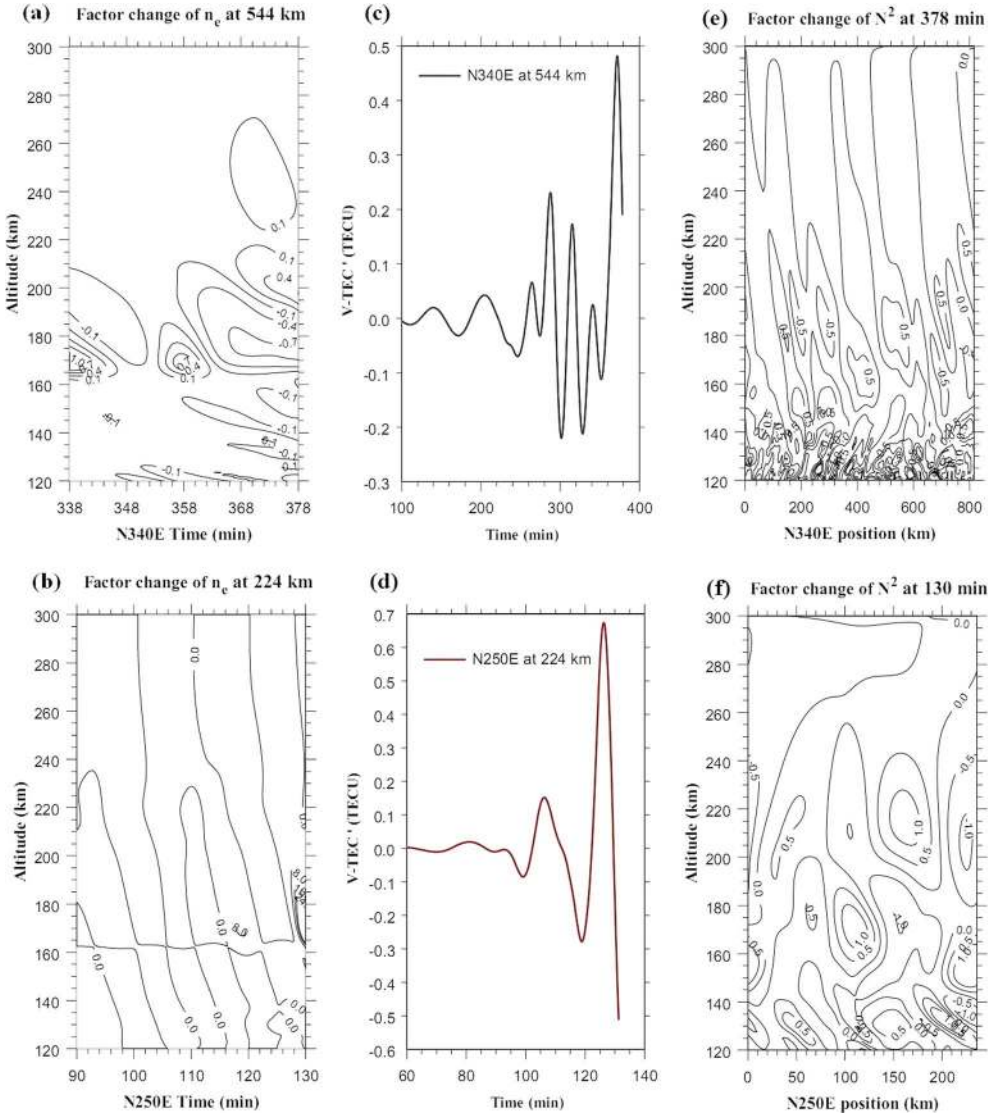

Figure 7. (a and b) Relative change of the electron number density (n_e), (c and d) time series of the V-TEC perturbations, and (e and f) relative change of the square Brunt-Väisälä frequency (N^2) due to AGWs propagating toward the N340°E (Figures 7a, 7c, and 7e) and N250°E directions (Figures 7b, 7d, and 7f) driven by the 2004 Sumatra tsunami.

To further reveal the altitude region where the convective instability forms, we examine the atmospheric stability, defined by the square of the Brunt-Väisälä frequency (N^2) [*Holton*, 2012]:

$$N^2 = \frac{g d\theta}{\theta dz} = \frac{g\left(dT/dz + g/c_p\right)}{T} \tag{12}$$

Here θ is the potential temperature, T is the temperature, c_p is the specific heat at constant pressure, $d\theta/dz$ is the vertical potential temperature gradient, and dT/dz is the vertical temperature gradient. If N^2 is less than zero, which occurs when the atmospheric lapse rate (dT/dz) exceeds the adiabatic lapse rate (g/c_p), the potential temperature decreases with height and convective instability occurs [*Hecht*, 2004].

In Figures 7e and 7f we show the relative change in N^2 from its initial value ($(N^2 - N_i^2)/N_i^2$), and hence, convective instability is indicated when this achieves a value of -1 or smaller. This ratio is shown in Figure 7e as a function of height and horizontal position at a time of 378 min for the wave propagating in the N340°E direction. It can be seen that this ratio never reaches -1 in the 120–300 km altitude region, and hence, this wave remains convectively stable. Figure 7f shows this quantity for the wave propagating toward the N250°E

direction at a time of 130 min. Convective instability (ratio < -1) is apparent near altitudes of 135, 170, and 205 km at horizontal positions exceeding 100 km. The earliest sign of the ratio less than -1 appears at about 126 min and at about 180 km altitude (not shown). The N250°E wave propagates upward through the *E*-region ionosphere (120 to 220 km) with a larger amplitude (see Figure 4a) and a smaller λ_z (see Figure 3a) than those of the N340°E wave. It forms an instability layer in this altitude region (see Figure 7f) and appears much earlier in the TEC fluctuation in its vertical propagation than the N340°E wave (see Figures 7a, 7b, 7c and 7d).

Although our analysis has indicated that the N340°E wave remains convectively stable, here we demonstrate that it becomes shear unstable. Usually, convective instability preempts shear instability [e.g., *Fritts and Rastogi*, 1985]. The criteria for shear instability involves the Richardson number, *Ri* [*Richardson*, 1920; *Gossard and Hooke*, 1975], to quantify the dynamical stability of the atmospheric region. *Ri* is a measure of the atmospheric stability to the destabilizing effects of wind shear. It is defined as

$$Ri = \frac{N^2}{(dU/dz)^2} = \frac{(g/T)\left(dT/dz + g/c_p\right)}{(dU/dz)^2}, \tag{13}$$

where *dU*/*dz* is the horizontal wind shear and others are as previously defined. *Richardson* [1920] originally claimed that the atmosphere would be unstable for *Ri* less than 1; however, later works have shown that in order to initiate the shear instability *Ri* needs to be less than 1/4 [*Miles*, 1961; *Howard*, 1961; *Chimonas*, 1970]. As reported by *Hines* [1971], *Gossard and Hooke* [1975], and *Hecht* [2004], once formed, instability can be maintained as long as *Ri* remains less than 1. The results of our analysis show that for the N340°E wave at about 378 min *Ri* is about 0.7 and 0.03 at about 125 and 105 km altitudes (not shown), respectively, where mean wind shears are large (see Figure 1a). The earliest sign of *Ri* less than 1 appears at about 358 min and at about 130 km altitude (not shown).

For the wave propagating toward the N250°E direction, the earliest sign of convective instability (when the relative change in $N^2 < -1$) appears at a time of about 126 min and at an altitude of about 180 km (not shown). At subsequent times, convective instability predominates for the N250°E wave and results in a different type of feature from that of the shear instability associated with the N340°E wave (Figure 6). The N250°E wave maintains values of *Ri* larger than 1 after about 126 min, in agreement with the finding of *Fritts and Rastogi* [1985] that convective instability preempts shear instability. Further detailed study on these wavefield instabilities requires a considerable future work; the interested readers are referred to the previous work of gravity wave saturation by *Fritts* [1989].

6. Discussion

6.1. 2004 Sumatra

Lee et al. [2008] reported on TID measurements from Arecibo that may have been associated with the 2004 Sumatra tsunami in the Indian Ocean. Two scenarios, described in their Figure 7, were postulated to explain these TID observations. For the first scenario involving propagation along a great circle path between Sumatra and Puerto Rico, our current findings suggest that the wave would propagate freely toward the N340°E direction spanning a horizontal distance of about 2246 km. This wave would subsequently break in the *E*-region ionosphere (see Figures 6a and 7a). Our results show that this wave would not be ducted because there is no upper boundary for such a duct (m^2 remains positive in the mesosphere and thermosphere, as shown in Figure 3a). Our findings therefore suggest that long-range wave propagation over a considerable distance (of about 18,000 km) between the epicenter and the observation site is highly unlikely.

Titov et al. [2005] determined the existence of tsunami disturbances in the Atlantic and Pacific Oceans beyond the source region. They further suggested a scenario involving a large U-turn path, as presented in Figure 7 of *Lee et al*. [2008]. The model results of *Titov et al*. [2005] indicated that the TIDs observed over Arecibo were generated in the vicinity of Puerto Rico by tsunami waves traveling toward the coast of Brazil. *Stevenson* [2005] estimated that the tsunami speed on the open Indian Ocean was about 200 m/s, while *Wilson* [2005] inferred a tsunami wavelength of about 500 km. Combined, they lead to an estimated tsunami wave period of about 41.7 min, consistent with the 40 min period tsunami wave propagating in the N250°E direction found by *Abe* [2006]. We have shown in Figure 6b that the 40 min AGW only propagates for about 130 min in the N250°E direction (equating to a horizontal distance of about 773 km), after which it

breaks in the *E*-region ionosphere (see Figure 7b). These findings lead us to conclude that the TIDs observed over Arecibo were attributable to the 40 min tsunami wave.

6.2. 2011 Tohoku

The 2011 Tohoku tsunami occurred in a region with densely distributed GPS receivers, the GPS Earth Observation Network (GEONET) in Japan. The results of our simulation shown in Figure 5a demonstrate that after 1 h following the tsunami onset, enhanced TID activity should first appear toward the northwest of the epicenter, which agrees with the TEC observations reported by *Galvan et al*. [2012] and the simulations by *Yu et al*. [2015]. Our current simulations demonstrate that the initial maximum TID activity occurs after an elapsed time of about 125 min and northwestward of the epicenter at a distance of about 900 km. The fact that this maximum TID activity is marginally contained within the GPS observable region would have allowed it to have been observed by the GEONET [*Galvan et al*., 2012].

The observations associated with the earlier tsunami in Sumatra [e.g., *Lee et al*., 2008] and the later tsunami in Tohoku [e.g., *Makela et al*., 2011; *Smith et al*., 2015; *Crowley et al*., 2016] affirm that the ionospheric response to this kind of natural hazard occurs on a global scale. Our simulations for the 2011 Tohoku tsunami also show an ionospheric response associated with long-range gravity wave propagation in the southeastward direction from the epicenter. We have shown that the latter maximum TID activity occurs after an elapsed time of about 230 min, and southeastward from the epicenter at a distance of about 3350 km. Because of the sparse population of GPS receivers in the deep Pacific Ocean, there have been no reported TIDs by GPS means that we are aware of that could confirm the existence of this latter long-range propagating gravity wave.

However, over the west coast of the U.S., *Crowley et al*. [2016] detected TIDs due to the tsunami after about 10 h at an azimuth of N105.2°E; the observed waveform is with the wave period of 15.1 min (near half of τ_d), a horizontal wavelength of 194.8 km (less than half of λ_h), and a horizontal phase speed of 233.0 m/s (close to the value of 243 m/s used here). These results are consistent with the far-field TID observations by *Makela et al*. [2011] after almost 5 h in airglow measurements over Hawaii.

7. Conclusions

We have used two numerical models describing the ionospheric responses to the atmospheric gravity waves that would likely be driven by the 2004 Sumatra and 2011 Tohoku tsunamis. Our results tend to argue against the plausibility that the 139 min gravity wave propagating toward the N340°E direction of the Sumatra epicenter was attributable to the TIDs observed over Arecibo, some 18,000 km from the source [*Lee et al*., 2008]. According to our simulations, the wave propagates freely for a horizontal extent of only about 2250 km, breaking afterward in the *E*-region ionosphere. Based upon our simulations and a combination of past researches due to *Abe* [2006], *Stevenson* [2005], and *Wilson* [2005], we attribute the 40 min tsunami wave propagating toward the N250°E direction from the Sumatra epicenter to the TIDs observed over Arecibo.

In addition to this, we have again found that the atmospheric gravity wave propagating toward the northwest from the Tohoku epicenter initially appeared about 1 h following the tsunami onset, while the wave propagating toward the southeast appeared later than this [*Galvan et al*., 2012; *Yu et al*., 2015]. The initial maximum TID activity would occur in about 2 h and northwestward at about 900 km from the epicenter. Serendipitously, this maximum occurs within the region observable by the GPS array (GEONET) (albeit marginally), as reported by *Galvan et al*. [2012]. Our simulations for wave propagation (and the associated ionospheric response) toward the southeast indicate that the time and distance associated with that propagation is over 4.5 h and 3900 km, respectively. This has not been confirmed by observations. However, we note that GPS receivers sparsely populate the deep ocean region of the Pacific east of the Tohoku epicenter, which could explain why the *F*-region TID activity we have simulated showing this later long-range propagation toward the southeast has not been observed.

Acknowledgments
Yonghui Yu was supported by the National Natural Science Foundation of China under grant 41174128. Data generated by models supporting the article are available for collaborative research upon request to the authors. We thank one of reviewers for highly recognizing our model efforts in the research.

References

Abe, K. (2006), Dominant periods of the 2004 Sumatra tsunami and the estimated source size, *Earth Planets Space*, *58*, 217–221, doi:10.1186/BF03353381.

Artru, J., V. Ducic, H. Kanamori, P. Lognonne, and M. Murakami (2005a), Ionospheric detection of gravity waves induced by tsunamis, *Geophys. J. Int.*, *160*, 840–848, doi:10.1111/j.1365-246X.2005.02552.x.

Artru, J., P. Lognonne, G. Occhipinti, F. Crespon, R. Garcia, E. Jeansou, and M. Murakami (2005b), Tsunami detection in the ionosphere, *Space Res. Today*, *163*, 23–27.
Chimonas, G. (1970), The extension of the Miles-Howard theorem to compressible fluids, *J. Fluid Mech.*, *43*, 833–836, doi:10.1017/S0022112070002781.
Crowley, G., I. Azeem, A. Reynolds, T. M. Duly, P. McBride, C. Winkler, and D. Hunton (2016), Analysis of traveling ionospheric disturbances (TIDs) in GPS TEC launched by the 2011 Tohoku earthquake, *Radio Sci.*, *51*, 507–514, doi:10.1002/2015RS005907.
Fritts, D. C. (1989), a review of gravity wave saturation processes, effects, and variability in the middle atmosphere, *Pure Appl. Geophys.*, *130*, 343–371.
Fritts, D. C., and P. K. Rastogi (1985), Convective and dynamical instabilities due to gravity wave motions in the lower and middle atmosphere: Theory and observations, *Radio Sci.*, *20*, 1247–1277, doi:10.1029/RS020i006p01247.
Galvan, D. A., A. Komjathy, M. P. Hickey, and A. J. Mannucci (2011), The 2009 Samoa and 2010 Chile tsunamis as observed in the ionosphere using GPS total electron content, *J. Geophys. Res.*, *116*, A06318, doi:10.1029/2010JA016204.
Galvan, D. A., A. Komjathy, M. P. Hickey, P. Stephens, J. Snively, Y. Tony Song, M. D. Butala, and A. J. Mannucci (2012), Ionospheric signatures of Tohoku-Oki tsunami of March 11, 2011: Model comparisons near the epicenter, *Radio Sci.*, *47*, RS4003, doi:10.1029/2012RS005023.
Gossard, E. E., and W. H. Hooke (1975), *Waves in the Atmosphere, Atmospheric Infrasound and Gravity Waves–-Their Generation and Propagation*, pp. 456 , Elsevier Sci, New York.
Hecht, J. H. (2004), Instability layers and airglow imaging, *Rev. Geophys.*, *42*, RG1001, doi:10.1029/2003RG000131.
Hedin, A. E. (1991), Extension of the MSIS thermosphere model into the middle and lower atmosphere, *J. Geophys. Res.*, *96*, 1159–1172, doi:10.1029/90JA02125.
Hedin, A. E., et al. (1996), Empirical wind model for the upper, middle and lower atmosphere, *J. Atmos. Terr. Phys.*, *58*, 1421–1447, doi:10.1016/0021-9169(95)00122-0.
Hickey, M. P., and K. D. Cole (1987), A quartic dispersion equation for internal gravity waves in the thermosphere, *J. Atmos. Terr. Phys.*, *49*, 889–899, doi:10.1016/0021-9169(87)90003-1.
Hickey, M. P., R. L. Walterscheid, M. J. Taylor, W. Ward, G. Schubert, Q. Zhou, F. Garcia, M. C. Kelley, and G. G. Shepherd (1997), Numerical simulations of gravity waves imaged over Arecibo during the 10-day January 1993 campaign, *J. Geophys. Res.*, *102*(A6), 11,475–11,489, doi:10.1029/97JA00181.
Hickey, M. P., G. Schubert, and R. L. Walterscheid (2009), Propagation of tsunami–driven gravity waves into the thermosphere and ionosphere, *J. Geophys. Res.*, *114*, A08304, doi:10.1029/2009JA014105.
Hickey, M. P., G. Schubert, and R. L. Walterscheid (2010a), Atmospheric airglow fluctuations due to a tsunami-driven gravity wave disturbance, *J. Geophys. Res.*, *115*, A06308, doi:10.1029/2009JA014977.
Hickey, M. P., R. L. Walterscheid, and G. Schubert (2010b), Wave mean flow interactions in the thermosphere induced by a major tsunami, *J. Geophys. Res.*, *115*, A09309, doi:10.1029/2009JA014927.
Hines, C. O. (1971), Generalization of the Richardson criterion for the onset of atmospheric turbulence, *Q. J. R. Meteorol. Soc.*, *97*, 429–439, doi:10.1002/qj.49709741405.
Holton, J. R. (2012), *An Introduction to Dynamic Meteorology*, 5th ed., Academic Press, San Diego, Calif.
Howard, L. N. (1961), Note on a paper of John W. Miles, *J. Fluid Mech.*, *10*, 509–512, doi:10.1017/S0022112061000317.
Kelley, M. C. (1989), *The Earth's Ionosphere*, Academic Press, San Diego, Calif.
Komjathy, A., D. A. Galvan, P. Stephens, M. Butala, V. Akopian, B. Wilson, O. Verkhoglyadova, A. Mannucci, and M. P. Hickey (2012), Detecting ionospheric TEC perturbations caused by natural hazards using a global network of GPS receivers: The Tohoku case study, *Earth Planets Space*, *64*, 1–8, doi:10.5047/eps.2012.08.003.
Lee, M. C., R. Pradipta, W. J. Burke, A. Labno, L. M. Burton, J. A. Cohen, S. E. Dorfman, A. J. Coster, M. P. Sulzer, and S. P. Kuo (2008), Did tsunami-launched gravity waves trigger ionospheric turbulence over Arecibo?, *J. Geophys. Res.*, *113*, A01302, doi:10.1029/2007JA012615.
Liu, J.-Y., Y.-B. Tsai, K.-F. Ma, Y.-I. Chen, H.-F. Tsai, C.-H. Lin, M. Kamogawa, and C.-P. Lee (2006), Ionospheric GPS total electron content (TEC) disturbances triggered by the 26 December 2004 Indian Ocean tsunami, *J. Geophys. Res.*, *111*, A05303, doi:10.1029/2005JA011200.
Liu, J.-Y., C.-H. Chen, C.-H. Lin, H.-F. Tsai, C.-H. Chen, and M. Kamogawa (2011), Ionospheric disturbances triggered by the 11 March 2011 M9.0 Tohoku earthquake, *J. Geophys. Res.*, *116*, A06319, doi:10.1029/2011JA016761.
Makela, J. J., et al. (2011), Imaging and modeling the ionospheric airglow response over Hawaii to the tsunami generated by the Tohoku earthquake of 11 March 2011, *Geophys. Res. Lett.*, *38*, L00G02, doi:10.1029/2011GL047860.
Marsh, D., S. C. Solomon, and A. E. Reynolds (2004), Empirical model of nitric oxide in the lower thermosphere, *J. Geophys. Res.*, *109*, A07301, doi:10.1029/2003JA010199.
Miles, J. W. (1961), On the stability of heterogeneous shear flows, *J. Fluid Mech.*, *10*, 496–508, doi:10.1017/S0022112061000305.
Occhipinti, G. E., A. Kherani, and P. Lognonné (2008), Geomagnetic dependence of ionospheric disturbances induced by tsunamigenic internal gravity waves, *Geophys. J. Int.*, *173*, 753–765, doi:10.1111/j.1365-246X.2008.03760.x.
Occhipinti, G., P. Lognonne, E. A. Kherani, and H. Hebert (2006), Three-dimensional waveform modeling of ionospheric signature induced by the 2004 Sumatra tsunami, *Geophys. Res. Lett.*, *33*, L20104, doi:10.1029/2006GL026865.
Occhipinti, G., L. Rolland, P. Lognonné, and S. Watada (2013), From Sumatra 2004 to Tohoku-Oki 2011: The systematic GPS detection of the ionospheric signature induced by tsunamigenic earthquakes, *J. Geophys. Res. Space Physics*, *118*, 3626–3636, doi:10.1002/jgra.50322.
Orlanski, I., and K. Bryan (1969), Formation of the thermocline step structure by large-amplitude internal gravity waves, *J. Geophys. Res.*, *74*, 6975–6983, doi:10.1029/JC074i028p06975.
Rees, M. H. (1989), *Physics and Chemistry of the Upper Atmosphere*, Cambridge Univ. Press, New York.
Richardson, L. F. (1920), The supply of energy from and to atmospheric eddies, *Proc. R. Soc. London A*, *67*, 354–373, doi:10.1098/rspa.1920.0039.
Rolland, L. M., G. Occhipinti, P. Lognonne, and A. Loevenbruck (2010), Ionospheric gravity waves detected offshore Hawaii after tsunamis, *Geophys. Res. Lett.*, *37*, L17101, doi:10.1029/2010GL044479.
Salmon, R. (2014), *Introduction to Ocean Waves*, Scripps Inst. of Oceanogr., Univ. of California, San Diego.
Schunk, R., and J. Sojka (1996), USU model of the global ionosphere, in *STEP: Handbook of Ionospheric Models*, edited by R. W. Schunk, SCOSTEP, Logan, Utah.
Smith, S. M., C. R. Martinis, J. Baumgardner, and M. Mendillo (2015), All-sky imaging of transglobal thermospheric gravity waves generated by the March 2011 Tohoku Earthquake, *J. Geophys. Res. Space Physics*, *120*, 10,992–10,999, doi:10.1002/2015JA021638.
Stevenson, D. (2005), Tsunami and earthquakes: What physics is interesting?, *Phys. Today*, *58*, 10.
Titov, V., A. B. Rabinovich, H. O. Mofjeld, R. E. Thomson, and R. I. Gonzalez (2005), The global reach of the 26 December 2004 Sumatra tsunami, *Science*, *309*, 2045–2048, doi:10.1126/science.1114576.

Vadas, S. L., J. J. Makela, M. J. Nicolls, and R. F. Milliff (2015), Excitation of gravity waves by ocean surface wave packets: Upward propagation and reconstruction of the thermospheric gravity wave field, *J. Geophys. Res. Space Physics*, *120*, 9748–9780, doi:10.1002/2015JA021430.

Walterscheid, R. L., and G. Schubert (1990), Nonlinear evolution of an upward propagating gravity wave: Overturning, convection, transience and turbulence, *J. Atmos. Sci.*, *47*(1), 101–125, doi:10.1175/1520-0469(1990)047<0101:NEOAUP>2.0.CO;2.

Walterscheid, R. L., and M. P. Hickey (2011), Group velocity and energy flux in the thermosphere: Limits on the validity of group velocity in a viscous atmosphere, *J. Geophys. Res.*, *116*, D12101, doi:10.1029/2010JD014987.

Wilson, M. (2005), Modeling the Sumatra-Andaman earthquake reveals a complex, nonuniform rupture, *Phys. Today*, *58*, 19.

Yamada, Y., H. Fukunishi, T. Nakamura, and T. Tsuda (2001), Breaking of small-scale gravity wave and transition to turbulence observed in OH airglow, *Geophys. Res. Lett.*, *28*, 2153–2156, doi:10.1029/2000GL011945.

Yu, Y., and M. P. Hickey (2007a), Time-resolved ducting of atmospheric acoustic-gravity waves by analysis of the vertical energy flux, *Geophys. Res. Lett.*, *34*, L02821, doi:10.1029/2006GL028299.

Yu, Y., and M. P. Hickey (2007b), Numerical modeling of a gravity wave packet ducted by the thermal structure of the atmosphere, *J. Geophys. Res.*, *112*, A06308, doi:10.1029/2006JA012092.

Yu, Y., and M. P. Hickey (2007c), Simulated ducting of high-frequency atmospheric gravity waves in the presence of background winds, *Geophys. Res. Lett.*, *34*, L11103, doi:10.1029/2007GL029591.

Yu, Y., M. P. Hickey, and Y. Liu (2009), A numerical model characterizing internal gravity wave propagation into the upper atmosphere, *Adv. Space Res.*, *44*(7), 836–846, doi:10.1016/j.asr.2009.05.014.

Yu, Y., Z. Yan, and M. P. Hickey (2015), Lower thermospheric response to atmospheric gravity waves induced by the 2011 Tohoku tsunami, *J. Geophys. Res. Space Physics*, *120*, 5062–5075, doi:10.1002/2015JA020986.